# Numerical studies of the interstellar medium on galactic scales

Pelupessy, F.I.

# Chapter 2

# Global models for the interstellar medium


## Abstract

Here we present a model of the interstellar medium (ISM) for use in simulations of galaxies. The model includes the main processes important for the neutral ISM. We include for the first time realistic photo-electric heating efficiencies and we solve for the ionization, invoking cosmic rays as ionizing agent. Using an N-body/SPH model of a star forming galaxy, we test models with different assumptions regarding cooling, heating and ionization. Star formation and feedback are included using simple but realistic prescriptions, resulting in self-regulated star formation. We test the influence of metallicity and cosmic ray flux. Varying the chemical abundances, we find that C depletion gives lower star formation, while Fe depletion decreases the amount of cold gas, leaving the star formation rate relatively unaffected. We also compare with previous models and show that if realistic photo-electric heating is used, stellar feedback is essential.


## 2.1 Introduction

Our understanding of the formation and evolution of galaxies is limited by our knowledge of the behaviour of the interstellar medium. Stellar dynamics and evolution are comparably well understood, and while practical problems remain there is a good understanding of phenomena. Of course, the nature of the dark matter in galaxies is a mystery , but to some extent this is a trivial problem as it only participates, almost by definition, in gravitational dynamics, and the distribution of dark matter on large scales can be reproduced in high detail through N-body simulations. It is not surprising then that a failure to match the observed number of dwarf galaxies and the mismatch in the properties of spirals and ellipticals of the current paradigm of structure formation in the universe, the $\Lambda$-cold dark matter ($\Lambda$CDM) model, is often attributed to a failure to account properly for physics of the ISM, especially the effects of feedback on the interstellar medium, rather than to defects of the basic properties of dark matter or the nature of gravitational forces in the model.

The state of the ISM determines where and when stars form. On the other hand, stars will seed the ISM with heavy elements and stir up the interstellar gas by putting in mechanical energy through the action of stellar winds, supernova (SN) explosions and UV radiation of young stars. From stellar evolution models the amount of metals, and energy produced are, except maybe for extremely low metallicity stars, well known input parameters.

The complexity of the dynamics and thermodynamics of the ISM have led to a prominence of computer modelling in galactic astrophysics. However the present models for the ISM used for galactic sized objects have been rather limited in the amount of physics that is included in these models. Most models represent the ISM as a smooth fluid, where the temperature of the gas, when not taken to be isothermal, is limited to be above $10^4$ K.

In this chapter we will explore global models for the ISM in galaxies, and discuss their implementation in a smoothed particle hydrodynamics (SPH) code. The models we develop can be used to simulate a wide variety of objects and would be useful whenever star formation is important on galactic scales, such as in studies of collisions of galaxies, galaxy formation scenarios or studies of star formation in spiral galaxies or dwarf galaxies.

## 2.2 The N-body/SPH method

The ISM models we present below will be implemented in a derivative of the N-body/SPH code TREESPH (Hernquist & Katz 1989, Gerritsen 1997, Bottema 2003). The gravitational forces are calculated using the Barnes-Hut algorithm (Barnes & Hut 1986) and gas dynamics using SPH (Monaghan 1992). The models we present here are not limited in their applicability to N-Body/SPH codes: they can be implemented in other types of hydrodynamic codes, like Eulerian grid codes. We have opted for a first implementation into an existing N-body/SPH code, as this method is well suited for problems with open boundary conditions and arbitrary geometries, like galaxy evolution and collision problems. N-body/SPH codes are well established tools for the theoretical astrophysicists, so we will only describe both methods concisely with an emphasis on the most relevant features of the implementation used.

### 2.2.1 Barnes-Hut treecode

The first ingredient of any self consistent model for galaxies is self gravity, as large scale gravitational instabilities are thought to drive star formation in galaxies. In the context of particle codes a number of different approaches are possible. The most precise solution is simply the brute force method of direct summation (DS) of the pairwise gravitational forces. This is costly, needing $\mathrm{O(N^2)}$ operations per force evaluation (although see Makino et al. 2003 for hardware solutions to this problem). Hence a number of approximate methods, sacrificing accuracy for speed, have been devised. We use the Barnes-Hut (BH) method (Barnes & Hut 1986). It is based on the following two concepts: 1) an approximation for the gravitational force of a group of particles by cutting off the multipole expansion after the quadrupole term, and 2) the hierarchical organization of particles in an oct-tree. A force evaluation for a particle is then done by recursive opening of the nodes in the tree, conditional upon a comparison of the size $\mathrm{l}$ of the node and the distance $\mathrm{d}$ to the centre of mass of the node:

$$\mathrm{l}/\mathrm{d} > \theta \tag{1}$$

where the parameter $\theta$ of the *cell opening criterion* controls the accuracy of the calculated gravitational forces. The BH method has been widely used in numerical N-body simulations, due to its $\mathrm{O}(\mathrm{N}\ \log \mathrm{N})$ scaling and its ability to be applied efficiently to general mass distributions. In astrophysics the method has found wide application in, for example, cosmological simulations, galaxy collision and star formation simulations. It has been shown that it is generally acceptable to use BH for collisionless N-body dynamics (Barnes & Hut 1989). However the classical BH opening criterion (1) can fail in exceptional circumstances (Salmon & Warren 1994). Also it was shown by Springel et al. (2001) that it will give large fractional force errors if particles are subjected to large cancelling forces such as those experienced in the smooth matter distributions found in the early universe. A similar problem may also occur for galaxy simulations, especially in the central regions of galaxies where particles experience large cancelling forces from the rest of the galaxy. Springel et al. (2001) propose an alternative opening criterion,

$$\mathrm{Ml}^4 > \alpha\, |\mathbf{a}|\, \mathrm{d}^6 \tag{2}$$

where $\mathrm{M}$ is the total mass contained in the node, $\mathbf{a}$ is an estimate of the acceleration, in practice this is the acceleration of the previous time step, and $\alpha$ the parameter controlling the accuracy of the force calculation. We have compared the accuracy of the BH criterion and the Springel criterion and found that the latter indeed gives smaller fractional force errors in the central regions of the galaxy.

### 2.2.2 Smoothed Particle Hydrodynamics

Smoothed Particle Hydrodynamics (Gingold & Monaghan 1977, Lucy 1977) is a particle based method for gas dynamics. It is based on an estimate of the local density of a continuous fluid respresented by a finite set of particles using a kernel function $\mathrm{W}(\mathrm{r}, \mathrm{h})$. Thus, for a set of particles with masses $\mathrm{m_i}$ and smoothing lengths $\mathrm{h_i}$ we have

$$\rho_\mathrm{i} = \sum_\mathrm{j} \mathrm{m_j} \mathrm{W}(|\mathrm{r_i} - \mathrm{r_j}|, \mathrm{h_i}) \tag{3}$$

for the density $\rho_\mathrm{i}$ at particle positions $\mathrm{r_i}$. The kernel function $\mathrm{W}$ is usually (and also here) taken to be the spline kernel of Monaghan & Lattanzio 1985:

$$\mathrm{W}(\mathrm{r}, \mathrm{h}) = \frac{1}{\pi \mathrm{h}^3} \begin{cases} 1 - \frac{3}{2}\left(\frac{\mathrm{r}}{\mathrm{h}}\right)^2 + \frac{3}{4}\left(\frac{\mathrm{r}}{\mathrm{h}}\right) & 0 \le \mathrm{r} \le \mathrm{h} \\ \frac{1}{4}(2 - \frac{\mathrm{r}}{\mathrm{h}})^3 & \mathrm{h} \le \mathrm{r} \le 2\mathrm{h} \\ 0 & \text{otherwise} \end{cases}$$

The idea of SPH is then to derive equations of motion for the particles starting from Eq. (3). This was originally done by substituting Eq. (3) into the equations of gas dynamics, but this is done more elegantly starting from the discretized Lagrangian for a compressible non dissipative flow, with adiabatic index $\gamma$ (Rasio 1999),

$$\mathrm{L} = \sum_{\mathrm{i}=1}^{\mathrm{N}} \mathrm{m_i} \left( \frac{1}{2}\mathrm{v_i^2} + \frac{1}{\gamma - 1}\mathrm{A_i}\rho_{\mathrm{i}}^{\gamma-1} \right) , \tag{4}$$

where $\mathrm{m_i}$ is the mass of particle i ($1 \leq \mathrm{i} \leq \mathrm{N}$), $\mathrm{v_i}$ its velocity, $\mathrm{A_i}$ is the entropic function, defined by ($\mathrm{P_i}$ being the pressure): $\mathrm{P_i} = \mathrm{A_i}\rho_{\mathrm{i}}^{\gamma}$. We will formulate the dynamic evolution of the internal energy in terms of this entropic function. The internal energy $\mathrm{u_i}$ itself is obtained through

$$\mathrm{u_i} = \frac{\mathrm{A_i}}{\gamma - 1}\rho_{\mathrm{i}}^{\gamma-1} \tag{5}$$

Treating the flow adiabatic for the moment and assuming constant smoothing lengths $\mathrm{h_i}$, it is easy to recover the SPH formalism from the Lagrangian equations of motion for $(\mathbf{q}, \mathbf{p}) = (\mathrm{r_1}, ..\mathrm{r_N}, \mathrm{v1}, .., \mathrm{v_N})$. Notice that the procedure we have outlined here is not specific for the kernel based density estimate of Eq. (3), indeed in Chapter 7 we will present an alternative method for gas dynamics by using the Delaunay Triangulation Field Estimator for the density, which is a much better density estimate in regions of high density contrasts or anisotropy. The dynamic range of conventional SPH is improved by the use of adaptive smoothing lengths. Normally this is done by choosing the $\mathrm{h_i}$ such that the number of neighbours within a smoothing length $\mathrm{h_i}$ is (more or less) constant for every particle. This introduces errors in energy and/or entropy conservation (Hernquist 1993, Nelson & Papaloizou 1993). This is because the variability of $\mathrm{h_i}$ introduces extra $\nabla \mathrm{h}$ correction terms into the dynamical equations, inclusion of which is, although possible (see Nelson & Papaloizou 1994), cumbersome. An alternative approach is to consider $\mathrm{h_i}$ as dynamic variables in the Lagrangian (4) and introduce constraints which will determine these extra variables (Springel & Hernquist 2002). Taking as the set of constraints

$$\phi = \frac{4\pi}{3}\mathrm{h_i^3}(\rho_{\mathrm{i}} + \tilde{\rho}) - \mathrm{M_r} = 0 \tag{6}$$

which (for constant density) is simply the requirement that the mass enclosed within a smoothing length is fixed. In this equation $\mathrm{M_r} = \bar{\mathrm{m}}\mathrm{N_{nb}}$ with mean particle mass $\bar{\mathrm{m}}$ and a target number of neighbours $\mathrm{N_{nb}}$. Comparing with Springel and Hernquist (2002) we add a term $\tilde{\rho}$ to limit the smoothing length $\mathrm{h_i}$. Without this term the smoothing length grows as $\mathrm{h_i} \rightarrow \infty$ when $\rho_i \rightarrow 0$, leading to a very high number of neighbours for particles on the edge of the simulation. A maximum $\mathrm{h_{i,max}^3} = 3\mathrm{M_r}/4\pi\tilde{\rho}$ leads to a minimum $\rho_{\mathrm{i,min}} = \mathrm{m_i}/\pi\mathrm{h_{i,max}^3} = 4\tilde{\rho}/3\mathrm{N_{nb}}$, which, to ensure errors due to poor sampling for particles with $\rho_{\mathrm{i}} \lesssim \tilde{\rho}$, are limited, is set to be lower than the intergalactic medium density by a suitable choice of $\tilde{\rho}$.

From the Lagrangian (4) and the constraints (6) the equations of motion follow in the usual way using Lagrange multipliers (for step by step derivation see Springel & Hernquist 2002). Because the potential of the Lagrangian in Eq. (4) is symmetric in the coordinate differences, total energy, entropy momentum and angular momentum will be conserved. The $\nabla \mathrm{h}$ terms are implicitly included to all orders. In our case this yields the following system of dynamic equations we solve in the code, including artificial viscosity terms ($W_{ij}(h_i) = W(|r_i - r_j|, h_i)$):

$$\frac{dv_i}{dt} = -\sum_{j=1}^{N} m_j \left\{ f_i \frac{P_i}{\rho_i^2} \nabla_i W_{ij}(h_i) + f_j \frac{P_j}{\rho_j^2} \nabla_i W_{ij}(h_j) + \Pi_{ij} \nabla \bar{W}_{ij} \right\} \tag{7}$$

with the $f_i$ defined by:

$$f_i = \left( 1 + \frac{h_i}{3(\rho_i + \tilde{\rho})} \frac{\partial \rho_i}{\partial h_i} \right)^{-1} \tag{8}$$

The artificial viscosity $\Pi_{ij}$ is necessary to smooth out discontinuities to resolvable scales, and we can take any one of the standard forms (Monaghan 1992, Hernquist & Katz 1989). Here, $\bar{W}_{ij} = W_{ij}(h_i) + W_{ij}(h_j)$ is a symmetrized form of the kernel. The thermodynamic state of the gas is determined by integrating the entropic function according to

$$\frac{dA_i}{dt} = -\frac{\gamma - 1}{\rho_i^{\gamma}} (\Gamma - \Lambda) + \frac{1}{2} \frac{\gamma - 1}{\rho_i^{\gamma - 1}} \sum_{j=1}^{N} m_j \Pi_{ij} v_{ij} \cdot \nabla_i \bar{W}_{ij} \tag{9}$$

Here $\Gamma$ and $\Lambda$ represent the external heating and cooling terms, which will be derived from a consideration of the physical processes that we want to include to model the ISM.

### 2.2.3 Some notes on implementation

The code we use is written in FORTRAN 90, and parallelised for use on shared memory architectures using OpenMP compiler directives.

We must solve Eq. (6) for the smoothing lengths $h_i$. This can be done efficiently using Newton-Raphson iteration, seconded by recursive bisection.

## 2.3 Physical processes of the ISM

Our model for the ISM will be mainly geared towards the representation of the neutral atomic phases of the ISM. Roughly speaking we will follow the ISM of our model galaxies as long as the temperature is higher than $100$ K and densities are greater than $100\ \mathrm{cm}^{-3}$. We will consider the formation and subsequent evolution of molecular clouds to be part of the process of star formation. The process of star formation in these clouds is not explicitly present in our model, but implicitly in the recipe for star formation (section 2.5.1).

A comprehensive model for the warm and cold neutral medium (WNM, CNM) that is similar to our model, albeit more extensive, was formulated by Wolfire et al. (1995, 2003). They explored the thermal equilibrium of the neutral ISM, in the context of a static model of the Milky Way. They concluded that their model was consistent with a number of observations, amongst which dust emission and [CII] line observations.

The main ingredients of our model are: cosmic ray regulated ionization, photoelectric heating from polycyclic aromatic hydrocarbons (PAHs) and small grains and

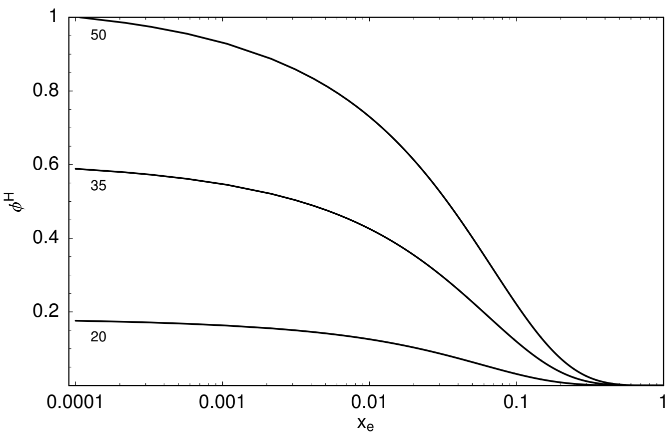


**Figure 2.1:** Secondary ionization function $\phi^{\mathrm{H}}$ for different electron energies. Curves are labelled with the corresponding energy of the secondary electron (in eV).

realistic cooling by a variety of atomic species. This improves on the treatment of previous models used in galactic simulations by not assuming a priori the ionization and by taking into account the efficiency decrease of photoelectric heating by grain charging. Also our cooling curves are more accurate and composed for arbitrary abundances, which allows us to explore the effect of variations of composition on the ISM.

### 2.3.1 Ionization

Even neutral interstellar gas retains some ionization. Gerritsen & Icke (1997) found that the results of their model depended on the ionization fraction $\mathrm{x_e} \equiv \mathrm{n_e}/\mathrm{n_H}$ assumed for temperatures below $\mathrm{T} \approx 14000$. For example for $\mathrm{x_e} = 0.1$ they found a star formation rate 4 times higher than for $\mathrm{x_e} = 0.01$ while the amount of cold gas was roughly ten times lower for the low $\mathrm{x_e}$ case. The reason for this is that the cooling power is proportional to $\mathrm{x_e}$. At low temperatures cooling is mainly due, if molecular gas is absent, to excitation of fine structure levels of neutral and ionized species. The excitation efficiency for collisions by electrons is much higher than that of neutral hydrogen, so for quite low ionization levels ($\mathrm{x_e} > 0.001$) the electron fraction will determine the amount of cooling. Gerritsen & Icke (1997) did not solve for the ionization, so they had to assume a value and for their standard model they settled for $\mathrm{x_e} = 0.1$. This seems to be reasonable for the solar neighbourhood (Cox 1990), however one would expect it to vary with local temperature and density, hence it is necessary to solve for ionization.

The CNM and WNM (with temperatures below $\mathrm{T} < 14000$) are too cold for the residual ionization to be explained by collisional ionization equilibrium (CIE). Additional sources of this ionization can be photo-,X-ray and Cosmic ray ionization. As the ISM is opaque to UV photons with energies higher than ionization potential of hydrogen, photo-ionization of hydrogen is generally constrained to HII regions, the immediate surroundings of bright UV sources, active galactic nuclei or star formation regions. We will lump the effect of HII regions together with the effects of stellar winds and supernovae as the mechanical luminosity of young stellar clusters. Photons with energies below 13.6 eV will propagate freely through the ISM, and any elements with ionization potentials less than 13.6 eV will be assumed to be at least singly ionized. Of the elements we include in our model these are C, Fe and Si. In practice the minimum ionization fraction in the simulation will be determined by the abundance of carbon, as it is the most abundant. Ionization of these species is also important for the cooling, in the next section we will see that $C^+$, $Si^+$ and $Fe^+$ are important coolants.

The main source of ionization in the neutral medium is probably collisions with cosmic rays. To calculate the resulting electron fraction $\mathrm{x_e}$, we solve for the ionization equilibrium of H and He only,

$$\alpha^{\mathrm{i}}_{\mathrm{coll}} \mathrm{n_e n_i} + \xi_{\mathrm{CR}} \mathrm{n_i} = \alpha^{\mathrm{i+1}}_{\mathrm{re}} \mathrm{n_e n_{i^+}} \tag{10}$$

with the $\mathrm{n_i}$ as the densities of $i$ =H, He, $He^+$ and $He^{++}$, $\alpha^{\mathrm{i}}_{\mathrm{coll}} = \alpha^{\mathrm{i}}_{\mathrm{coll}}(\mathrm{T})$ and $\alpha^{\mathrm{i}}_{\mathrm{re}} = \alpha^{\mathrm{i}}_{\mathrm{re}}(\mathrm{T})$ the appropriate collisional ionization and recombination rates. For these we take the fits of Voronov (1997)[1]. Here, $\xi_{\mathrm{CR}}$ is the total cosmic ray ionization rate, which is determined by the primary ionization rate $\zeta_{\mathrm{CR}}$ multiplied by a factor accounting for the secondary ionizations by the energetic electrons produced in primary ionization events (Wolfire et al. 1995),

$$\xi_{\mathrm{CR}} = \zeta_{\mathrm{CR}} \left(1 + \phi^{\mathrm{H}}(\mathrm{E}, \mathrm{x_e}) + \phi^{\mathrm{He}}(\mathrm{E}, \mathrm{x_e})\right). \tag{11}$$

The functions $\phi^{\mathrm{H}}(\mathrm{E}, \mathrm{x_e})$ and $\phi^{\mathrm{He}}(\mathrm{E}, \mathrm{x_e})$ give the number of secondary ionizations of hydrogen and helium per primary ionization. These depend on the energy $\mathrm{E}$ of the secondary electron (we take a typical value of 35 eV) and the electron fraction $\mathrm{x_e}$. We use the analytic fits for $\phi^{\mathrm{H}}$ and $\phi^{\mathrm{He}}$ provided in the appendix of Wolfire et al. (1995). Qualitatively, the number of secondary electrons increases with $\mathrm{E}$, as expected, while for increasing $\mathrm{x_e}$, it decreases (the secondary electron will loose its energy more easily through Coulomb interactions for high ionization fractions). For the primary ionization rate we take a standard value of

$$\zeta_{\mathrm{CR}} = 1.8 \times 10^{-17} \mathrm{s}^{-1}. \tag{12}$$

Note that the primary cosmic ray ionization rate $\zeta_{\mathrm{CR}}$ is mainly due to particles with energies below 100 MeV, which are shielded from direct observation by the heliosphere (extrapolation from Pioneer and Voyager data yields a rate of $\zeta_{\mathrm{CR}} = 3 \times 10^{-17}$, Webber 1998) and also expected to vary substantially due to their low travelling lengths. Presumably their production sites are regions of star formation, and calculation of the propagation of these cosmic rays is complicated. The canonical value (12) comes from chemical modelling of molecular clouds (Van Dishoeck & Black 1986) and may not be appropriate for the diffuse ISM (McCall et al. 2003). So the actual value of the cosmic ray flux that is appropriate is uncertain (however this does not mean that details as (11) are superfluous, because it introduces a feedback of $\mathrm{x_e}$ on the ionization rate that is present regardless of the actual value for $\zeta_{\mathrm{CR}}$).

The system of Equations (10) is easily solved by iterating over $\mathrm{x_e}$, in practice we also tabulate its solutions for quick referencing by interpolation in temperature $\mathrm{T}$

[1] http://www.pa.uky.edu/~verner/atom.html

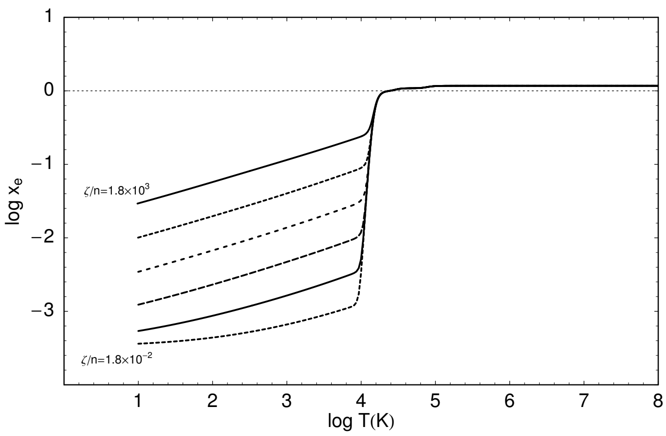


**Figure 2.2:** Ionization fraction $x_e = n_e/n$ for different values of $\zeta_{CR}/n$, increasing from $\zeta_{CR}/n = 1.8 \times 10^{-2}$ to $\zeta_{CR}/n = 1.8 \times 10^{3}$ in factors of 10.

and $\zeta_{CR}/n$. In Fig. 2.2 we have plotted the resulting ionization fraction for solar metallicities.

We solve for the ionization to get an estimate of $x_e$. Metals will not contribute significantly and hence we do not solve for their ionization. The abundance of the different ionized species needed for the cooling rates (see below) will be assumed to be in CIE. For calculation of CIE a more complete set of processes including charge exchange is considered (included in the *Doric* package, Raga et al. 1997, Mellema & Lundqvist 2002).

Apart from cosmic ray ionization a seizable contribution is expected from X-ray ionizations. We will not consider these separately, because of the above mentioned uncertainties in the cosmic ray ionization rate, and because the physical process of X-ray ionization is similar to cosmic ray ionization.

### 2.3.2 Cooling processes

A heated, partially ionized gas cools through the conversion of kinetic energy into luminosity by collision processes, and the efficiency of cooling is a sensitive function of the composition of the gas. The cooling in the low density limit can be approximated by

$$\Lambda = n^2 \Lambda^\star(T) \tag{13}$$

For the cooling curve $\Lambda^\star(T)$ a number of pre-compiled cooling curves for specific metallicities exist (e.g. Dalgarno & McCray 1972, Sutherland & Dopita 1993). We calculate the cooling curve for general abundances using recent atomic data. In Fig. 2.3 we have plotted the cooling curve

$$\Lambda^\star(T) = \sum_{i,j} X_{ij} \left( x_e L^{e}_{X_{ij}}(T) + L^{H}_{X_{ij}}(T) \right) \tag{14}$$

for solar and $0.2\times$ solar metallicity. The functions $L^{e}_{X_{ij}}$ and $L^{H}_{X_{ij}}$ give the cooling power for collisions with electrons and neutral hydrogen of ionization stage $j$ of element $i$

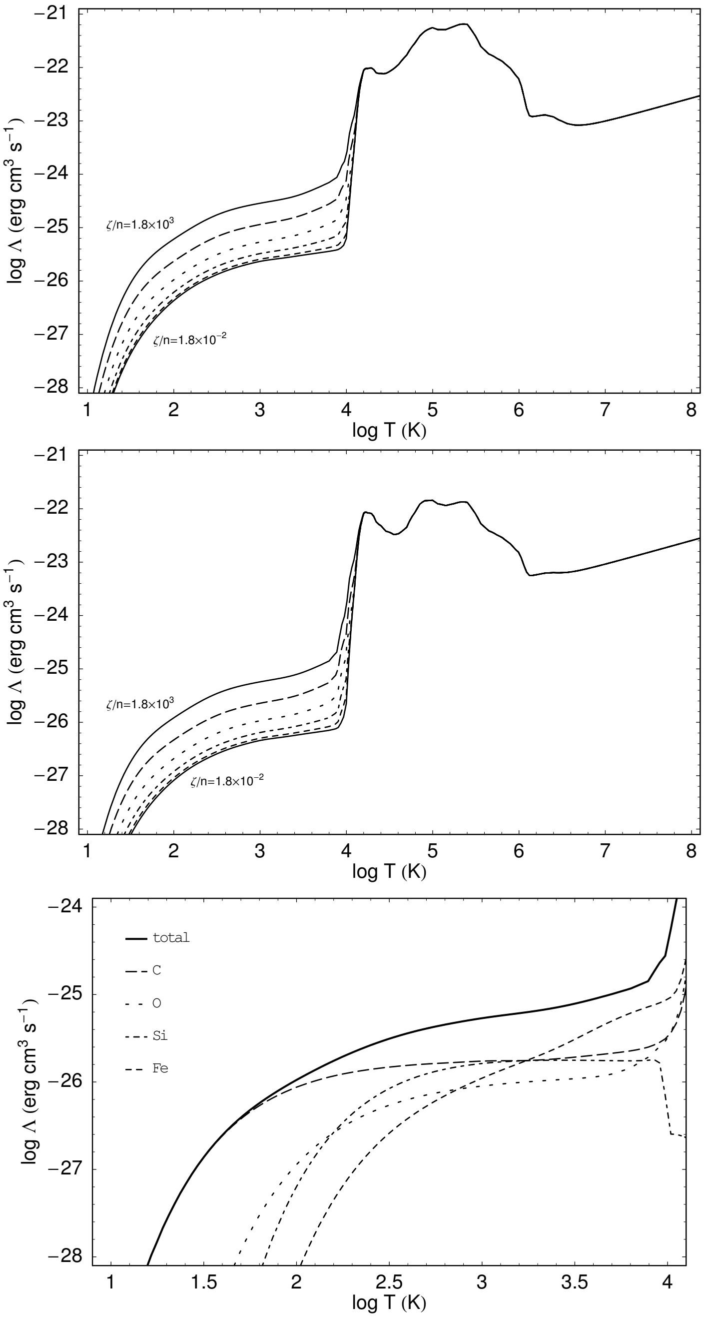


**Figure 2.3:** Cooling curves. **Top panel:** Cooling curves for $Z = Z_\odot$, labelled with values of $\zeta/n$ as in Fig. 2.2. **Centre panel:** Cooling curves for $Z = 0.2 \times Z_\odot$, idem. **Bottom panel:** contributions to cooling curves for the most important elements, for $\zeta_{CR}/n = 18$ and $Z = Z_\odot$.

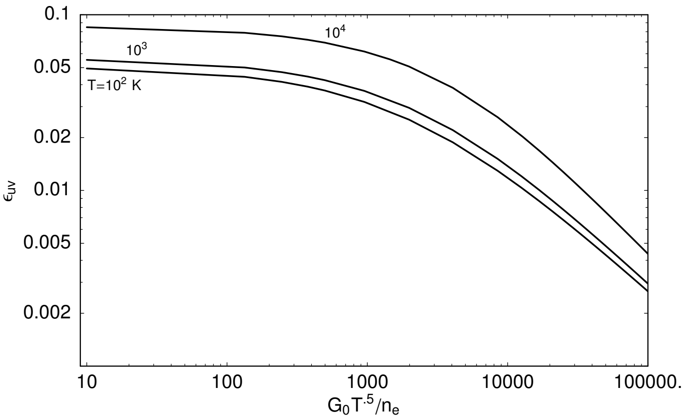


**Figure 2.4:** Full UV heating efficiency $\epsilon_{\rm UV}$.

with a relative abundance $\rm X_{ij}$. We take $\rm L^{e}_{X_{ij}}$ from a recent compilation of atomic data from the *Doric* package (Raga et al. 1997, Mellema & Lundqvist 2002 ), while we calculate $\rm L^{H}_{X_{ij}}$, using the *Popratio* program (Silva & Viegas 2001). Also in Fig 2.3 we have plotted the contributions of the various elements to the cooling for the most important coolants. For solar metallicity carbon (in the form of CII) is the main coolant at low temperatures ($\rm T < 1000$ K). Iron is dominant at temperatures between $3000$ and $10000$ K. Si can also be a substantial coolant at intermediate temperatures (around $1000$ K).

Note that apart from the dependency on the composition of the gas, cooling is strongly dependent on the ionization fraction, because $\rm L^{e}_{X_{ij}}$ is typically a factor $1000$ bigger than $\rm L^{H}_{X_{ij}}$.

### 2.3.3 Heating processes

The most important heating mechanism in the neutral ISM is photoelectric heating from small grains and PAHs (Watson 1972): UV radiation will heat gas in the presence of dust through the ejection of electrons from these particles. We will use the results of modelling by Bakes & Tielens (1994) to calculate this heating. The heating for a radiation field $\rm G_0$, normalised to Habing's ($1.6 \times 10^{-3}$ erg cm$^{-2}$ s$^{-1}$, 1968), is given by

$$\Gamma = 10^{-24}\,\epsilon_{\rm UV} {\rm n}\,({\rm Z/Z_\odot})\,{\rm G_0}\ \ {\rm erg\ cm^{-3}\ s^{-1}}, \tag{15}$$

where the heating efficiency $\epsilon_{\rm UV}$ is fitted by

$$\epsilon_{\rm UV} = \frac{4.9\times10^{-2}}{1+[\xi_{\rm gr}/1925]^{0.73}} + \frac{3.7\times10^{-2}\left({\rm T}/10^4\right)^{0.7}}{1+[\xi_{\rm gr}/5000]} \tag{16}$$

with $\xi_{\rm gr} = {\rm G_0 T^{0.5}/n_e}$ the grain charge parameter. This parameter is proportional to the rate of ionization of the dust grains divided by the recombination rate. As discussed in Wolfire (1995), for small values of $\xi_{\rm gr}$ the dust grains are mainly neutral, whereas for large values of this parameter the grains become positively charged, and

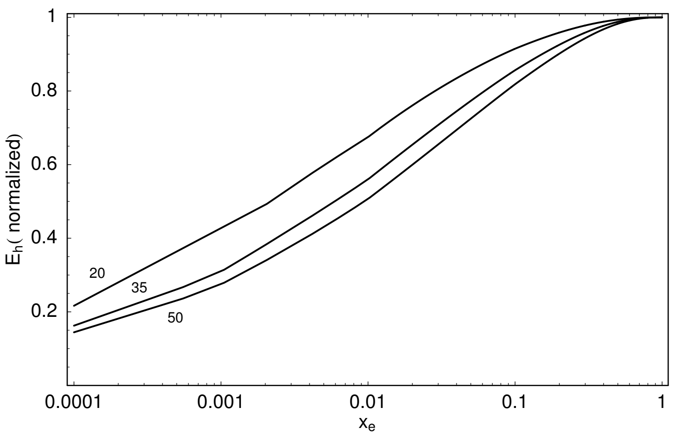


**Figure 2.5:** Cosmic ray heating function $E_h$. Plot of the fraction of the secondary electron energy used for heating. Curves are labelled with secondary electron energy.

electrons need to overcome an extra potential barrier to get expelled from the grains. This lowers the energy available for heating the gas, which decreases the efficiency for increasing $\xi_{gr}$ (Fig. 2.4). This has important implications for the heating rates in our model, effectively reducing the strength of the radiative feedback for high radiation fields to $\propto G_0^{0.27}$. So compared to Gerritsen & Icke (1997) and Bottema (2003), who took a constant efficiency, the UV radiation feedback will be less important for establishing star formation equilibrium. Note also that in this case the heating becomes a strong function of ionization, as high ionization reduces grain charging.

The heating of Eq. (15) scales with metallicity (assuming the dust-to-gas ratio scales with Z), UV field, density and takes into account grain charging. We do not take into account the finer points of dust physics, notably the dependence of the heating on the shape of the spectral energy distribution of the impinging radiation field and the dependence of the heating on size and shape distribution of the dust grains. Both effects can change the heating rate by 25%, when varying the parameters under reasonable constraints (Wolfire 1995). In principle the distribution of the grain sizes, shapes etc could come out of a model for the formation, processing and destruction of dust grains and PAHs, but clearly this is a very complicated problem. We will just assume the same grain distribution to be present everywhere.

The UV field needed in Eq. (15) is calculated from the distribution of stars, analogous to the way the gravitational forces are calculated. Dust extinction is not taken into account explicitly, although we do roughly model the extinction of UV light from young stellar clusters by the remnants of the natal clouds by increasing the emission of UV light from 25% to 100% of the nominal luminosity over a period of 4 Myr.

Normally photoelectric heating dominates over X-ray and cosmic ray heating, but this is not the case in the outer parts of galaxies where both density and radiation field drop. In these regions we will provide for heating by including cosmic ray heating, which for a primary ionization rate $\zeta_{CR}$ is given by

$$\Gamma = n\zeta_{CR}E_h(E, x_e) \tag{17}$$

The function $E_h(E, x_e)$ gives the heat deposited for every primary electron of energy $E$ (of typically 35 eV), given in Wolfire (1995). We have plotted this function in Fig. 2.5.

In principle X-ray heating may also be important, but as its effect and magnitude is similar to that of cosmic ray heating (and this term is subject to some uncertainty, see discussion in section 2.3.1), we do not include it separately.

### 2.3.4 Molecular gas

We will not consider the formation of molecular gas in this chapter. However in view of the importance of molecular gas, both as fuel for the formation of stars, and as a diagnostic tool in extra-galactic studies of star formation, we will here give an overview of the relation of molecular gas and the gaseous phase of our simulation. In Chapter 6 we will investigate the formation of the most important molecule, $H_2$, in some detail.

A direct implementation of $H_2$ formation from first principles in current galaxy scaled computer simulations is, both from the viewpoint of the necessary resolution as from the viewpoint of necessary physics, impractical. In our simulation the physics of molecular cloud formation is considered to be part of the star formation process, captured in a basic but plausible model (see below). A result of this approach is that the star formation rates will not be set by molecular cloud physics, but at a larger scale: by the surface density of the gas, cooling properties of the neutral medium and large scale instabilities. This is consistent with the prevailing view of star formation (Elmegreen 2002). The mass that is contained in the molecular phase will be present in the cold phase in our simulation, and thus, while assessing the amount of cold gas resulting from our simulations, one must keep in mind that this includes a considerable amount of what would be molecular gas.

Note that diffuse $H_2$ gas is also absent in our model. This may be a more serious omission. Diffuse $H_2$ may be present at abundances of $10^{-3} - 10^{-4}$ in the neutral medium (Richter et al. 2001) and at this level it could affect the cooling of the neutral medium substantially, as the cooling efficiency of $H_2$ gas is about a factor $10^3$ higher than for our neutral gas (Le Bourlot et al. 1999).

## 2.4 Equilibrium models

The different heating and cooling processes we have discussed in section 2.3 constitute a reasonably complex model for the ISM. It is certainly more realistic than most previous models that have been used in galaxy simulations, as it attempts to include the cold and warm phases of the neutral ISM. To get an idea of the properties of the resulting ISM it is instructive to explore the thermal equilibrium state of our model and compare it to the previous models of Gerritsen & Icke (1997), Bottema (2003) and also to the equilibrium models of Wolfire et al. (1995).

The models we present will be incorporated into a fully dynamical simulation, where we solve for the thermal evolution of the gas. To see to what extent the thermal equilibrium state is relevant as a description of the state of the ISM, we can compare the timescales of different processes. As we will demonstrate below, there are a range of processes in the ISM that are acting on timescales comparable to the timescales associated with the thermal evolution of the gas.

A region of cold gas subjected to an increase in UV radiation will quickly heat to a temperature of $T_{eq} = 10^4$ K in a time

$$t_{heat} = \frac{\rho u_{eq}}{\Gamma} = \frac{3/2kT_{eq}}{\Gamma} \approx \frac{10^6}{(Z/Z_\odot)\,G_0}\ \text{yr} \tag{18}$$

The time a region of density $\rho$ and internal energy $u = 3/2kT$ needs to return to equilibrium after a significant perturbation is given by the cooling time,

$$t_{cool} = \frac{\rho u}{\Lambda} = \frac{3/2kT}{f_H n \Lambda^\star} \tag{19}$$

which gives roughly $t_{cool} \approx 10^5$ yr ($n = 10$ cm$^{-3}$, $T = 100$ K) for the CNM and $t_{cool} \approx 10^7$ yr ($n = 0.1$ cm$^{-3}$, $T = 10^4$ K) for the WNM.

Variations in the local UV field were studied by Parravano et al. 2003. They found variations on timescales of $10^{7-8}$ yr. This is comparable to timescales in the WNM but much slower than the timescales of the CNM. A similar conclusion holds for supernova perturbations. Wolfire et al. (2003) estimated for the characteristic time of these that $t_{shock} = 5.3 \times 10^6$ yr.

So we see that under quiescent (solar neighbourhood) conditions thermal equilibrium is a reasonable assumption for the CNM and marginally good for the WNM, whereas for more active regions this assumption will become increasingly questionable, especially for the WNM but also for the CNM, since the frequency of most of the perturbing agents scales with star formation rate. A large fraction of out-of-equilibrium gas is consistent with recent HI absorption line studies, which find that a substantial fraction (around 50%) of the WNM is in an unstable temperature range, and thus presumably not in equilibrium (Heiles & Troland 2003, Kanekar 2003).

### 2.4.1 Heating and ionization assumptions

To explore the effect of the different heating and ionization processes that are new to our ISM model and to compare these to previous work, we explore a number of different models, designated A B C and D, of increasing complexity. For the moment we consider solar metallicity. The first of these models (model A) is the same, except for the cooling, as the model used in Gerritsen & Icke (1997): a constant heating efficiency ($\epsilon_{UV} = 0.05$) and a constant ionization fraction ($x_e = 0.1$). Model B has the heating efficiency of Eq. (16), while retaining constant ionization. Model C has constant heating efficiency while solving for ionization and finally model D is our complete model solving for the ionization and using the full heating efficiency. Fig. 2.6 shows for these four models the equilibria of pressure, temperature, electron fraction and heating (=cooling) rate.

The plots in this figure show that as density increases, the equilibrium state of the gas changes from a high temperature ($T = 10^4$ K) at low densities, to a low temperature ($T < 100$ K) at high densities. For all four models there is a density domain in between where the negative slope of the P-n relation indicates that the gas is unstable to isobaric pressure variations, the classic thermal instability (Field 1965). We

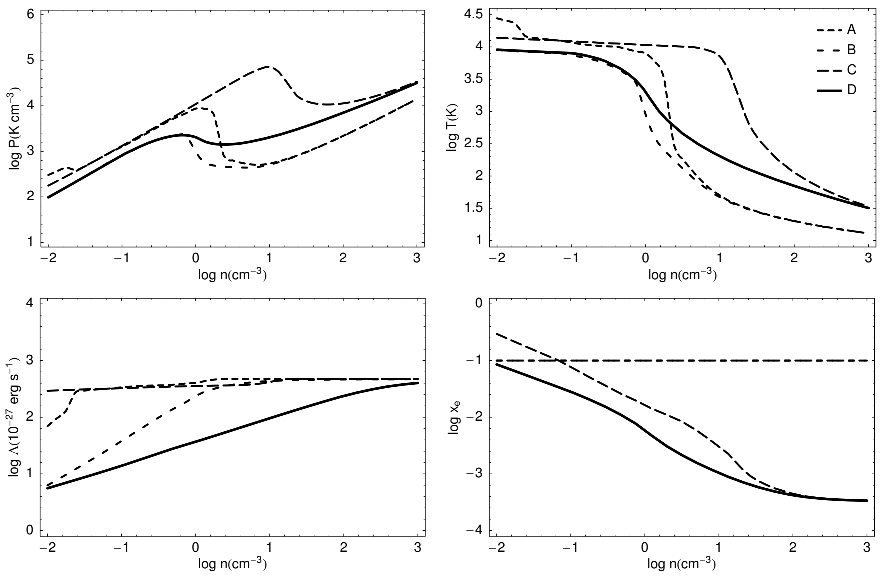


**Figure 2.6:** Thermal equilibrium properties of models A,B,C and D. Shown are (in order: top left, top right, bottom left and bottom right) the pressure, temperature, cooling rate and ionization fraction in thermal equilibrium as a function of density. In the plot results are shown for $Z = Z_\odot$ and $G_0 = 10$.

see that the models which do not solve for the ionization (A and B) seriously overestimate the ionization at high densities and thus overestimate the cooling resulting in lower temperatures. The models which do not use the full heating efficiency (A and C) overestimate the heating, especially at low densities, hence these have higher temperatures at low density. The total effect is that the range of pressures for which the ISM is unstable will be much greater in the simpler models.

If we compare Fig. 2.6 to Fig. 3 of Wolfire et al. (1995) we see that our model D is very similar, showing very similar trends for electron fraction and heating rate. Hence our model captures most of the essential physics of the Wolfire et al. model.

In a complete simulation the conditions of UV and supernova heating will vary from place to place. This will change the relations of Fig. 2.6. So next we will explore the effect of variation of UV and cosmic ray heating.

### 2.4.2 UV field and Cosmic rays

In Fig. 2.7 we have plotted an overview of model D for three different values of the UV field $G_0$. Note that as the UV field increases the density and pressure for which a cold phase is possible shift up. Also, if some region is collapsing, then, as long as no star formation is happening, the UV field may be expected to stay more or less constant and since density increases gas will stay at the lines of constant heating in for example the n-T relation. Then, as stars form, heating will suddenly increase, and

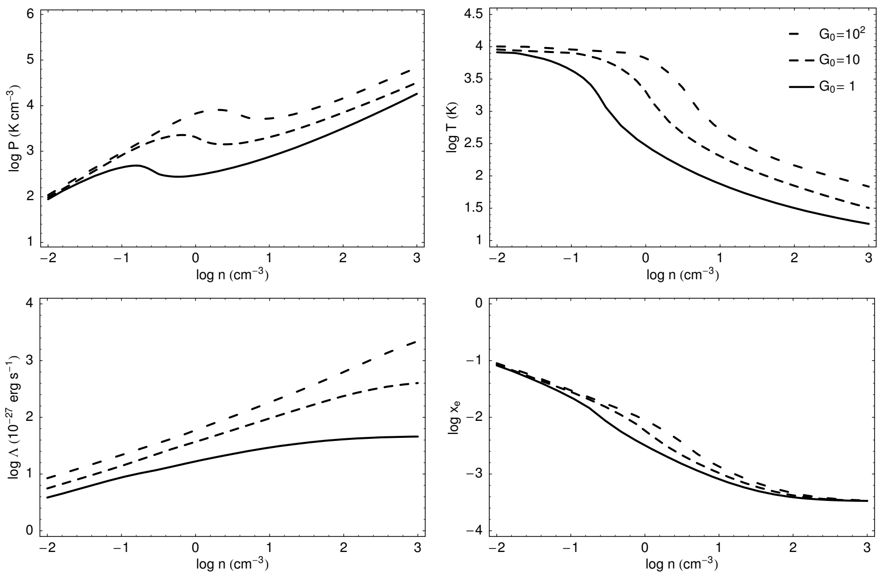


**Figure 2.7:** Thermal equilibrium properties of model D: varying UV heating. $\mathrm{Z} = \mathrm{Z}_\odot$.

gas will 'move up' quickly to a new $\mathrm{G}_0$ curve , cf. (18).

An increase in cosmic ray flux shows a similar pattern: In Fig. 2.8 we have plotted the pressure-density relation for different cosmic ray fluxes. A high value for the cosmic ray ionization rate may very well be appropriate: for diffuse clouds in the solar neighbourhood McCall et al. (2003) found that a value of the cosmic ray ionization rate of up to $\zeta_{\mathrm{CR}} = 1.2 \times 10^{-15}$ was necessary to account for the observed abundance of $\mathrm{H}_3^+$.

### 2.4.3 Varying chemical composition

In Fig. 2.9 we show the effect of varying the chemical composition. A lower metallicity shifts the unstable region to higher density and pressure, while also extending the range of unstable pressures. Note that the ISM model is still relatively insensitive to variations in metallicity. This is because we scale the dust-to-gas ratio, and thus the heating efficiency, with metallicity. Both cooling and heating are to first order proportional to metallicity. In Fig. 2.10 we show the $\mathrm{Z} = \mathrm{Z}_\odot/5$ model in more detail. Pressure, temperature and electron fraction are similar to the model for solar metallicity, although the cooling rate shifts down. The cooling and heating times (19) and (18) scale inversely with metallicity. So while varying the metallicity has relatively little effect on the equilibrium state, it will affect our full dynamical modelling.

In Fig. 2.9 we have also plotted the effect of separately depleting Fe+Si and C, as they affect cooling at completely different temperatures. Note that depletion of iron enlarges the pressure range of thermal instability, while depletion of carbon has the effect of heating the cool phase.

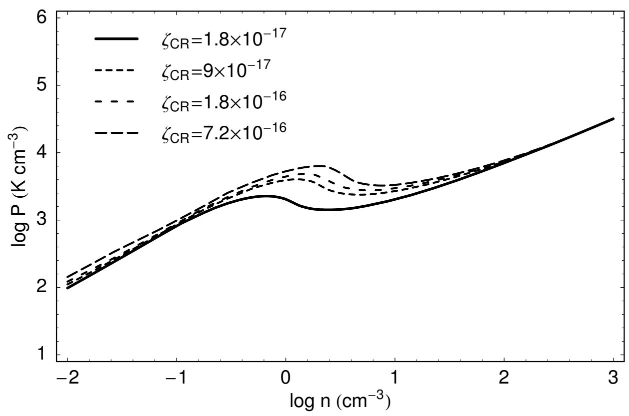


**Figure 2.8:** Equilibrium pressure-density relation for different cosmic ray fluxes, $\mathrm{G}_0 = 10$.

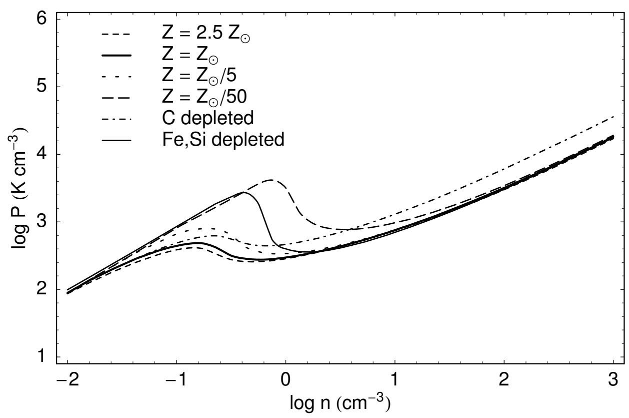


**Figure 2.9:** Equilibrium pressure-density relation for different chemical compositions, $\mathrm{G}_0 = 1$.

## 2.5 Star formation and its effects

From the point of view of our simulation star formation is micro physics that is not resolved. The formation of stars in dense clouds of the interstellar medium is a complex process that is still very much an active field of research, and there is no general theory to predict the star formation rate of a given region of the ISM. However from observations and theory some key processes are identified. Probably the most influential observational relation is the *Schmidt law* (Schmidt 1959): the empirical finding that the star formation rate (SFR) of disk galaxies varies with gas surface density $\sigma_{\mathrm{g}}$ as $\mathrm{SFR} \propto \sigma_{\mathrm{g}}^{1.5}$. It can be explained by assuming that gravitational instabilities play the regulating role in star formation on large scales (Elmegreen 2002). Furthermore it seems that star formation is a self regulating process: young star clusters will disrupt the cloud in which they form by heating it with UV photons and by stirring the gas mechanically through the action of stellar winds and supernova feedback.

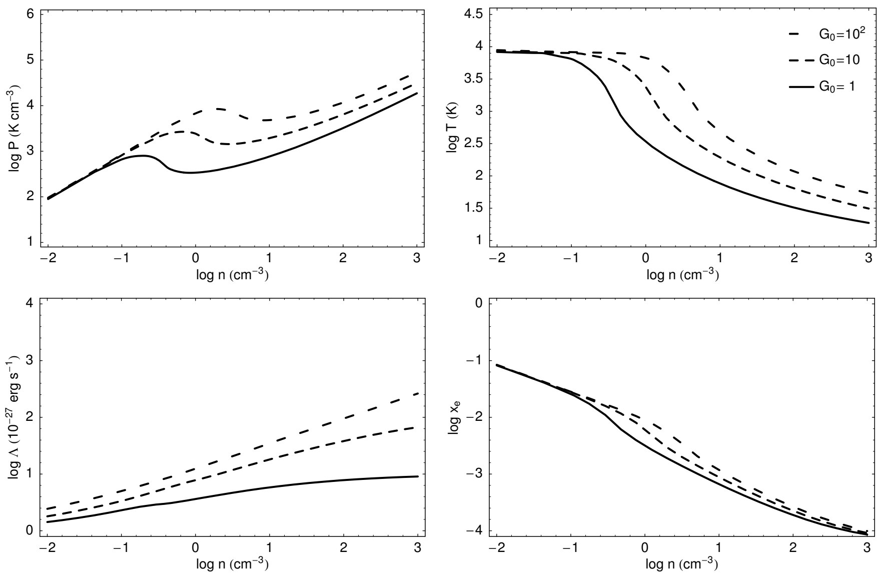


**Figure 2.10:** Thermal equilibrium properties of model D with $Z = Z_\odot/5$, varying $G_0$

### 2.5.1 Star Formation

We use the star formation recipe of Gerritsen & Icke (1997). A region is considered unstable to star formation if the local Jeans mass $M_J$,

$$M_J = \frac{\pi\rho}{6}\left(\frac{\pi s^2}{G\rho}\right)^{3/2} \tag{20}$$

with $s$ the sound speed, is smaller than the mass of a typical molecular cloud $M_{ref}$,

$$M_J < M_{ref}. \tag{21}$$

The rate of star formation is set to scale with the local free fall time,

$$\tau_{sf} = f_{sf} t_{ff} = \frac{f_{sf}}{\sqrt{4\pi G\rho}}. \tag{22}$$

The delay factor $f_{sf}$ accounts for the fact that collapse of molecular clouds is inhibited by either turbulence or magnetic fields (Mac Low & Klessen 2004, Shu et al. 1987). Its value is uncertain, but from observations a value $f_{sf} \approx 10$ seems reasonable (Zuckerman & Palmer 1974).

There are many different ways to let stars form locally on the timescale given by Eq. (22). One way to achieve this, followed by Gerritsen & Icke (1997) is to wait for a time $\tau_{sf}$ and then proceed to form stars. Another is just to assign a probability $1 - \exp(-\Delta t/\tau_{sf})$ for star formation in a time step $\Delta t$. We have not found any compelling reason to prefer one method over the other. There are however also subtle numerical differences between the two methods: in the stochastic case star formation may also be delayed beyond $\tau_{\rm sf}$, and where this is the case the unstable region may collapse to higher densities than it would in the fixed delay case. The fixed delay case, on the other hand tends to synchronize star formation over regions that become unstable at the same time, which leads to a sudden onset of star formation, for example in the beginning of the simulation. We will note whenever a choice of either one has a substantial impact on the results.

Once a gas particle is determined to be forming stars, a fraction $\epsilon_{\rm sf}$ of the mass is converted to stars. This sets a minimum to the star formation efficiency (a neighbourhood of gas particles of about 64 particles that has become capable of star formation will thus form at least a fraction $\epsilon_{\rm sf}/64$ of stars). The actual efficiency of star formation is determined by the number of stars needed to quench star formation locally by the UV and SN heating and is determined by the cooling properties of the gas and the energy input from the stars.

Thus the local star formation rate will be given by

$$\frac{{\rm d}\rho_\star}{\rm dt} = -\frac{{\rm d}\rho_{\rm gas}}{\rm dt} = \frac{\epsilon_{\rm sf}}{\tau_{\rm sf}}\rho_{\rm JU} \tag{23}$$

where $\rho_{\rm JU}$ indicates the 'Jeans unstable' gas, satisfying (21). The effective timescale for star formation is $\tau_{\rm eff} = \tau_{\rm sf}/\epsilon_{\rm sf} = {\rm f_{sf}t_{ff}}/\epsilon_{\rm sf}$, so different combinations of $\rm f_{sf}$ and $\epsilon_{\rm sf}$ will give the same star formation rate. In case of a fixed delay time (Gerritsen & Icke method), it is appropriate to take a constant mass fraction $\epsilon_{\rm sf}$ for the newly formed star particles, while in the stochastic method we can form star particles of fixed mass, and thus bigger $\epsilon_{\rm sf}$ as gas particles become lighter, as long as we increase $\rm f_{sf}$ accordingly.

The recipe is certainly not unique, we have based our choice on the following considerations: it is simple and based on presence of substructure and the driving role of gas self gravity, and it reproduces the Schmidt law without actually imposing it (Gerritsen & Icke 1997). It does assume substructure to be present (actually its assumption is more restrictive still, namely that substructure is mainly at $\rm M_{ref}$ sized clouds, but this is not overly important). For this type of simulation one is always restricted by the limited ability to follow the star formation process, so we are forced to adopt a phenomenological description at some level.

Another concern that could be addressed is that the SF according to this recipe is independent of metallicity, other than that induced by the metallicity dependence of the cooling. If cloud collapse is regulated by magnetic fields (Shu et al. 1987), a more detailed dependence of the delay factor $\rm f_{sf}$ on for example ionization may be appropriate.

We assume the stellar initial mass function (IMF) to be universal. We take a Salpeter IMF with a lower mass cutoff of $0.1\ \rm M_\odot$ and an upper mass cutoff of $100\ \rm M_\odot$. The shape of the IMF determines the amount of heavy stars, and thus the amount of UV and supernova feedback. If the IMF would vary according to local conditions this will have its effect on star formation. Observations are consistent with a universal IMF over a wide range of ISM conditions, however there are some hints that for high radiation fields and/or low metallicities relatively more high mass stars are formed (e.g. Lamers et al. 2002).

The star formation recipe we employ has an additional advantage: namely, it prevents the simulation from violating the resolution requirements for self gravitating SPH of Bate & Burkert (1997) and Whitworth (1998). For SPH the local Jeans mass should be bigger than the local mass resolution,

$$\mathrm{M_J > Nm_{SPH}}, \tag{24}$$

otherwise artificial clumping or inhibition of clumping may occur. This condition is just Eq. (21), *if* $\mathrm{M_{ref}}$ is chosen equal to the local mass resolution, $\mathrm{M_{ref} = Nm_{SPH}}$ (N is the number of SPH neighbours, and $\mathrm{m_{SPH}}$ the mass of SPH particles). We will do so, and our simulation will thus follow collapse and fragmentation of the ISM from the WNM to the CNM, but at a certain point (Eq. 21) the simulation can no longer reliably follow this process. At this point further assumptions regarding the details of star formation enter through Eq. (22). In practice this limit lies at a very physically relevant region of parameter space, namely at temperatures and densities where molecular clouds should form in the CNM. So our simulation tracks the evolution of the WNM and CNM up to a point where a phase of the ISM forms that can be trusted to form stars, at efficiencies that are somewhat constrained by observations. As we increase resolution and decrease $\mathrm{m_{SPH}}$ we can decrease $\mathrm{M_{ref}}$ and follow the collapse further.

### 2.5.2 Stellar model

We calculate the FUV luminosities of the stellar particles from the age and metallicity of the stars and Bruzual & Charlot (1993, and updated) population synthesis models. For this the integrated flux between $912$ and $2100$ Å is calculated from single burst models with a salpeter IMF with a low mass cutoff of $0.1\ \mathrm{M_\odot}$ and high mass cutoff of $100\ \mathrm{M_\odot}$. It is not entirely clear if interpolation in metallicity from the coarse grid data available is the best strategy, so in case we run a model with a metallicity different from the Bruzual & Charlot models we just take the synthesis model with the closest matching metallicity. We roughly account for the extinction of UV light of young stars by their natal cloud by increasing the flux from 25% at birth to 100% at 4 Myr, in accordance with counts of UV sources in the neighbourhood of star forming clouds (Parravano et al. 2003, and references therein).

### 2.5.3 Feedback

In addition to heating by UV radiation, stars heat the surrounding gas through the injection of energy by stellar winds, supernovae and the expansion of HII regions. We will consider these three effects to constitute the *mechanical luminosity* of our stellar particles. Stars heavier than $8\ \mathrm{M_\odot}$ are generally assumed to explode as supernovae with energies of $10^{51}$ erg, so together with stellar lifetimes and the IMF, this fixes the contribution from supernovae. The contribution of stellar winds can be estimated from stellar evolution modelling and theoretical and observational mass loss rates and terminal velocities, (e.g. Leitherer et al. 1999). If we look at the mechanical energy output of a stellar cluster (Fig. 2.11) we see that stellar winds dominate early on, but the integrated luminosity indicates that they contribute less than about 6% to the the total mechanical energy. For metallicities lower than solar this value would be even lower.

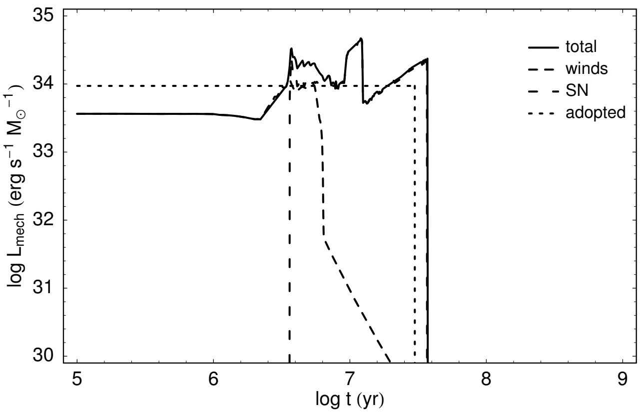


**Figure 2.11:** Mechanical energy output from stellar cluster. Plotted as a function of age of a single burst of star formation at $\mathrm{Z} = \mathrm{Z}_\odot$ are the separate contributions from stellar winds (short dashed) and supernovae (long dashed), as well as the total mechanical luminosity(drawn) from Leitherer et al. (1999). The dotted line indicates the mechanical luminosity of the stellar particles adopted in our simulation.

While the mechanical energy output of stars can thus be estimated with reasonable accuracy, it has proven to be difficult to include the effects of feedback completely self-consistently in galaxy sized simulations of the ISM. The reason for this is that the effective energy of feedback depends sensitively on the energy radiated away in thin shells around the bubbles created. This will mean that the effect of feedback is not reliable unless prohibitively high resolution is used. In SPH codes there have been conventionally two ways to account for mechanical feedback: by changing the thermal energy input and by acting on particle velocities. Both are unsatisfactory, as the thermal method suffers from over cooling (Katz 1992) and the kinetic method seems to be too efficient in disturbing the ISM (Navarro & White 1993). Here we use a new method based on the creation at the site of young stellar clusters of *pressure particles* that act as normal SPH particles in the limit that the mass of the particle $\mathrm{m} \rightarrow 0$, for constant energy (see Chapter 3 for more details). For the energy injection rate we take $\dot{\mathrm{E}} = \epsilon_{\mathrm{sn}} \mathrm{n}_{\mathrm{sn}} \mathrm{E}_{\mathrm{sn}} / \Delta \mathrm{t}$, with supernova energy $\mathrm{E}_{\mathrm{sn}} = 10^{51}$ erg, an efficiency parameter $\epsilon_{\mathrm{sn}} = 0.1$, number of supernova $\mathrm{n}_{\mathrm{sn}}$ per solar mass of stars formed of $\mathrm{n}_{\mathrm{sn}} = 0.009$ and an active period $\Delta \mathrm{t} = 3 \times 10^7$ yr (approximately the lifetime of a $8\ \mathrm{M}_\odot$ star). The efficiency $\epsilon_{\mathrm{sn}}$ thus assumes that 90% of the energy is radiated away, a value which comes from more detailed simulations of the effect of supernova and stellar winds on the ISM (Silich et al. 1996), and is also used in other simulations of galaxy evolution (e.g. Semelin & Combes 2002, Springel & Hernquist 2002, Buonomo et al. 2000). In Fig. 2.11 we have also plotted the mechanical luminosity of the stellar particles in our model. Note that the fact that we approximate the mechanical luminosity by a constant will not introduce big errors, as the energy of the pressure particles is a time integrated quantity.

## 2.6 Putting it all together

The combination of hydrodynamics, self-gravity and the ISM models of section 2.4 with our star formation and feedback recipes will set up a self regulated ISM. The distribution of temperature, density, etc. of the gas and amount and location of star formation will be the outcome of the interaction between the competing processes of heating and cooling, feedback and collapse. We will test this global model for the ISM of star forming galaxies by applying it in a simulation of a suitable galaxy.

### 2.6.1 Initial conditions

For our purposes we need a simple model galaxy. We construct a three component model of a typical star forming disk galaxy with a gaseous disk, a stellar disk and a dark halo.

The stellar disk has a mass of $10^{10}$ $\mathrm{M_\odot}$ and is constructed to be approximately exponential,

$$\rho_{\mathrm{disk}}(\mathrm{R,z}) = \frac{\Sigma_0}{2\mathrm{h_z}} \exp(-\mathrm{R/R_d}) \mathrm{sech}^2(\mathrm{z/h_z}), \quad (25)$$

for a central surface density $\Sigma_0 = 5 \times 10^8$ $\mathrm{M_\odot}$/kpc$^2$, disk scale $\mathrm{R_d} = 1.8$ kpc and a vertical scale-height $\mathrm{h_z} = 0.4$ kpc. The disk is constructed using the approximate three-integral disk distribution function of Kuijken & Dubinski (1995). The initial ages of the stellar particles are distributed according to an exponentially decaying star formation rate with a burst time of 5.2 Gyr, resulting in a current star formation rate for this galaxy of $\mathrm{SFR} = 0.2$ $\mathrm{M_\odot}$/yr.

For the gaseous disk we take a radial surface density

$$\Sigma = \Sigma_\mathrm{g}/(1 + \mathrm{R/R_g}), \quad (26)$$

with central density $\Sigma_\mathrm{g} = 0.008 \times 10^9$ $\mathrm{M_\odot}$/kpc$^2$ and radial scale $\mathrm{R_g} = 3$ kpc, truncated at 14 kpc. Thus it has a total mass of $\mathrm{M_{gas}} = 1.05 \times 10^9 \mathrm{M_\odot}$. Initially the gas is given a temperature $\mathrm{T} = 10^4$ K.

Both the stellar and gas disk are represented by $\mathrm{N} = 10^5$ particles. The dark halo is represented by a static potential and has a Navarro, Frenk & White (1997, NFW) profile

$$\rho_{\mathrm{halo}}(\mathrm{r}) = \frac{\rho_\mathrm{s}}{(\mathrm{r/r_s})(1 + \mathrm{r/r_s})^2}, \quad (27)$$

$\rho_\mathrm{s} = 4 \times 10^7$ $\mathrm{M_\odot}$/kpc$^3$ and $\mathrm{r_s} = 6$ kpc. The dark to baryonic mass ratio is thus $\mathrm{M_{dark}/M_{baryon}} = 5$ at the edge of the gas disk.

### 2.6.2 Galaxy models without supernova feedback

First we will compare the models A, B, C and D of section 2.4.1 without the effect of mechanical feedback. We let the model galaxy evolve, using the different ISM models as well as our star formation and SN feedback processes. Quickly, after about 200 Myr, a steady state develops where the distribution of temperature and density of the gas changes only marginally due to the consumption of gas by star formation.

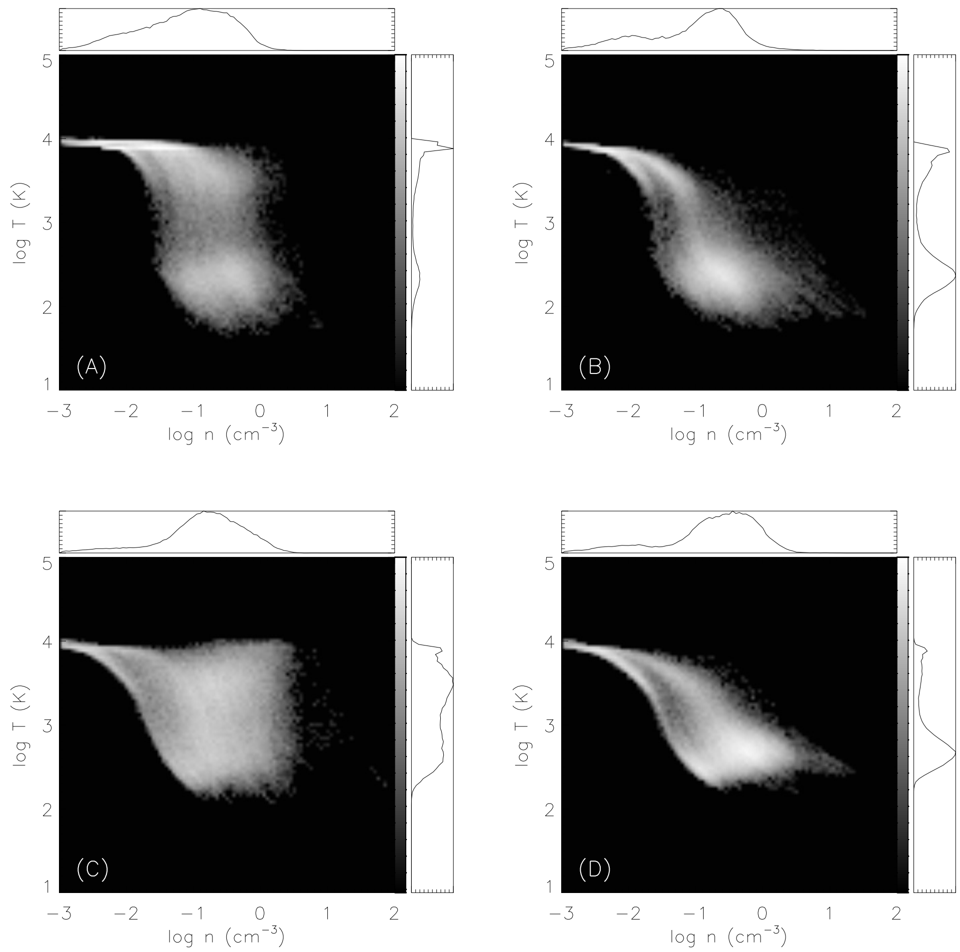


**Figure 2.12:** Temperature-density distribution of simulation runs of model A, B, C and D w/o feedback. Histograms of the corresponding quantity are plotted to the right and above the frames. These histograms are linear and scaled to the maximum bin.

In Fig. 2.12 we have plotted the density-temperature diagram for the different models. If we look at the panel of model A, which is equivalent to the model of Gerritsen & Icke 1997, we recognize the two phase structure as found by them. Most of the gas is at temperatures of around $\mathrm{T} = 10^4$ K. Note that gas cools to about $\mathrm{T} = 100$ K, but densities stay below $\mathrm{n} = 10$ cm$^{-3}$, due to the limited resolution. The star formation rate of $\mathrm{SFR} \approx 0.6\ \mathrm{M}_{\odot}$/yr is similar to that found by Gerritsen & Icke (Fig 2.13). We also find that the distribution of gas and stars has similar properties as in their simulations, more specifically: cold gas is confined to the midplane of the galaxy, showing a flocculent spiral structure caused by stretching of collapsing structures due to differential rotation.

However if we look at the temperature and density distribution of model D we

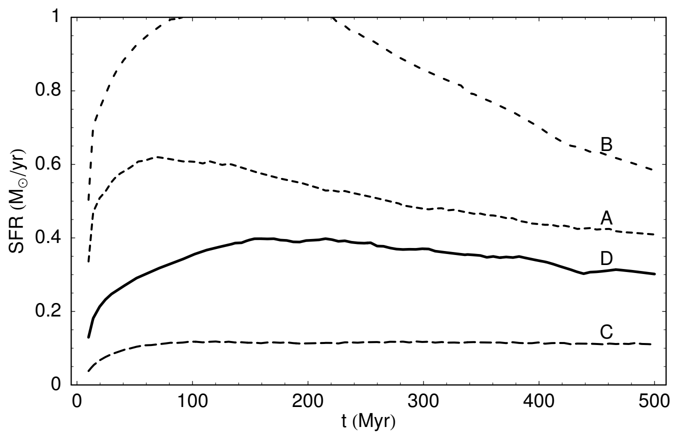


**Figure 2.13:** Star formation rate of simulation runs of model A, B, C and D without feedback.

see a qualitatively different picture: most of the gas at high densities is now concentrated at low temperature. Comparing with model B and C we see that this is due to the effect of using heating efficiency (16) rather than using a constant efficiency. Grain charging flattens the dependency (16) at high UV fields to $G_0^{0.27}$. In this case heating from stellar UV radiation is not sufficient to heat the gas back to $10^4$ K. The effect of lower ionization keeps gas in models C and D at somewhat higher minimum temperatures compared to the constant ionization cases of model A and B.

If we look at the star formation rates of the model galaxies, we see that models A and D have similar star formation rates peaking at $\mathrm{SFR} = 0.6\ \mathrm{M}_\odot$/yr and $\mathrm{SFR} = 0.4\ \mathrm{M}_\odot$/yr. Although a bit on the high side, these are reasonable SFR, considering the uncertainties present in the modelling. For model B, the peak star formation rate $\mathrm{SFR} = 1.2\ \mathrm{M}_\odot$/yr is clearly too high, and also results in a gas consumption time that is very short ($\approx 1$ Gyr). Model C has very low star formation rate, due to the combination of overestimated heating and realistic cooling. We see that the effect of ionization and grain charging are cancelling out for model D giving it a similar star formation rate as model A.

### 2.6.3 Galaxy models with SN-feedback

We ran the same models again, but this time including supernova feedback. Fig. 2.14 and 2.15 give the corresponding temperature-density plots and star formation rates. In this case additional heating from the SN masks the effect of grain charging. Although models with the complete heating efficiency still have a higher cool gas fraction, heating is sufficient to heat the gas back to $10^4$ K, allowing for cycling between WNM and CNM: cold gas is heated and will expand back to low densities. If we look at the star formation rates we see that for model C the addition of SN heating makes very little difference, while lowering the star formation rate substantially for the other models.

For the remainder, we take model D with SN feedback as our standard model and compare to it the effects of varying abundances and cosmic ray fluxes.

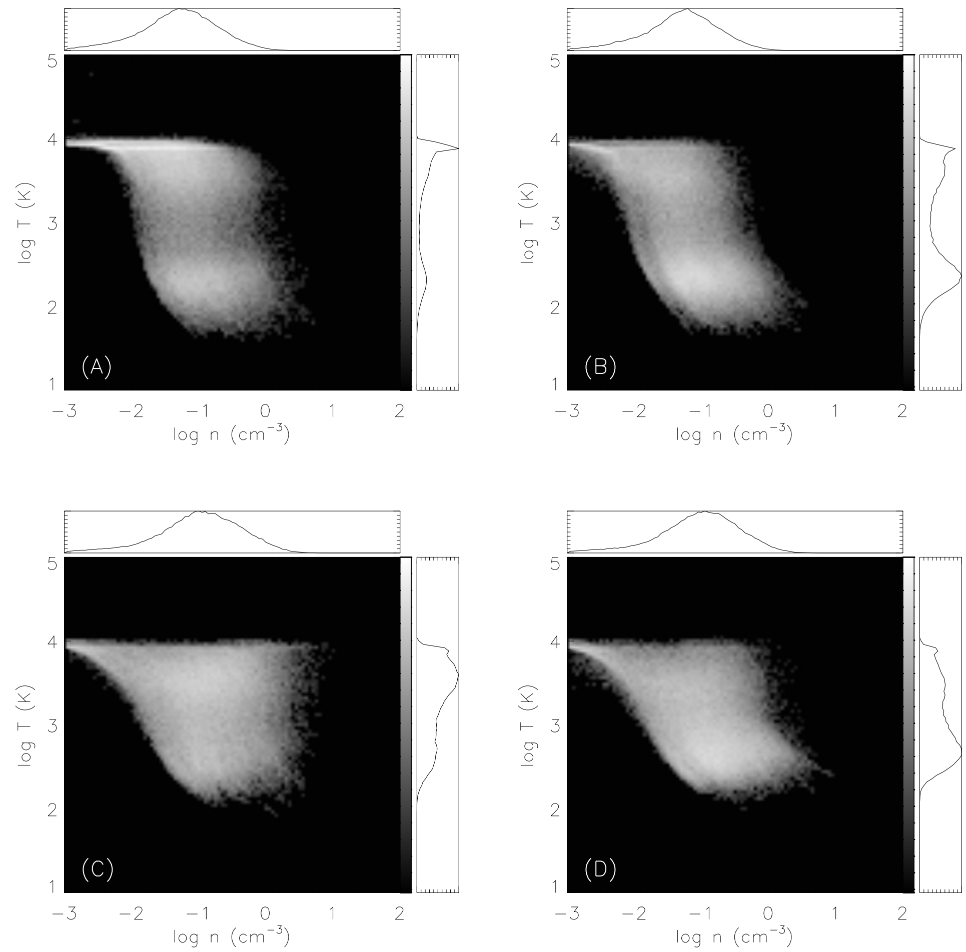


**Figure 2.14:** Temperature-density distribution of simulation runs of model A, B, C and D with feedback.

### 2.6.4 The effect of chemical composition

We ran a set of four simulations with varying chemical composition, but otherwise the same as the above model D. Two of these we ran with higher and lower metallicity scaled from solar: $Z = 2.5 \times Z_{\odot}$ and $Z = Z_{\odot}/5$, the remainder were the Fe+Si and C depleted models of section 2.4.3. Note that for the models where we use scaled metallicities we use a corresponding set of stellar models, while for the depleted models we use the standard solar metallicity population synthesis.

In Fig. 2.16 we have plotted the temperature-density distribution for these runs. The low metallicity run shows a markedly different temperature distribution, especially at low densities, being much warmer. This is due to cosmic ray heating, which becomes relatively important as metallicity goes down (we scale dust content, and thus grain heating with Z). The distribution of the high metallicity model is very sim-

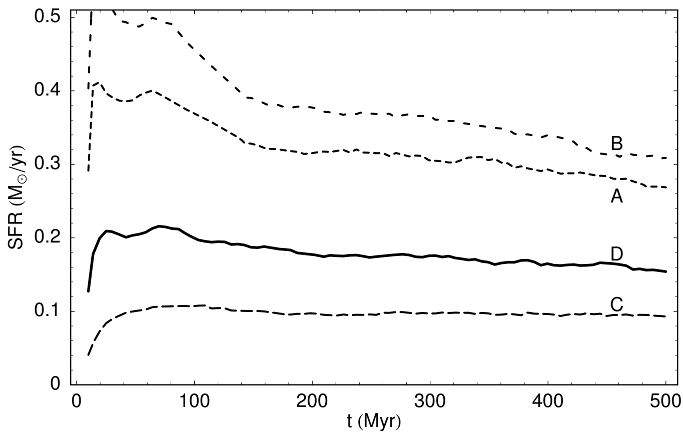


**Figure 2.15:** Star formation rate of simulation runs of model A, B, C and D with feedback.

ilar to solar metallicity. A plot of the star formation rates of these models, Fig. 2.17, shows that *both* have lower star formation rates. This suggests that the star formation efficiency attains a local maximum at solar metallicity. The decrease at higher metal contents is probably due to the fact that the UV flux is higher (by a factor 2-3) for Bruzual & Charlot (1993) stellar models with $\mathrm{Z} = 2.5 \times \mathrm{Z}_\odot$ compared to $\mathrm{Z} = \mathrm{Z}_\odot$ (as is the case for low metallicity).

Comparing the Fe and C depleted runs in Fig. 2.16, we see that for the Fe depleted run there is very little cold gas. The depletion of C has an effect mainly on the star formation rate, see Fig. 2.18, since C affects the cooling at low temperatures. Note that for the low iron simulation the star formation is also affected, but less so than one would expect from the temperature distribution: the abundance of C affects the star formation rate, while the Fe abundance affects the relative amounts of warm and cold neutral gas.

### 2.6.5 Cosmic rays and the star formation threshold

As discussed in section 2.3.1 the heating and ionization from cosmic rays and X-rays are not well constrained. Hence to see what the effect of this uncertainty is on our model we have run additional models with 5 and 40 times higher cosmic ray fluxes. The effect of increasing the cosmic ray flux is to heat the gas at low densities, while not affecting gas at high densities much (Fig. 2.19). An increase by a factor of 5 still has a minor effect on the total star formation, while a factor 40 increase only lowers the star formation rate with about 50%. If we look at the radial star formation density (Fig. 2.21) we see that star formation in the centre is decreased little for higher cosmic ray rates, but that the edge of star formation moves in as cosmic ray flux increases. This is consistent with models for the threshold of star formation that explain it as a thermal effect (Schaye 2004, Elmegreen & Parravano 1994). As was pointed out by Schaye (2004), the fact that the cold phase is absent beyond a certain radius means that the disk is gravitationally stable beyond this radius and thus star formation quenched. Note that in our model galaxy the radius of the edge of the star

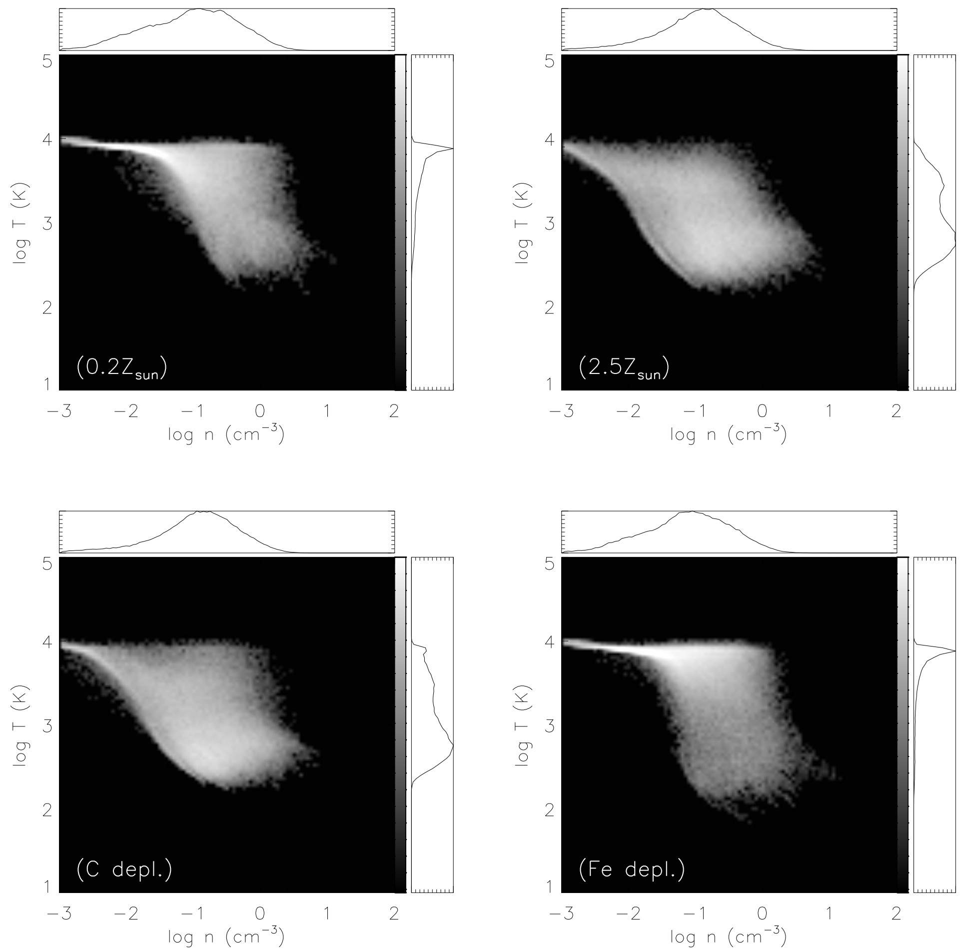


**Figure 2.16:** Temperature-density distribution of simulation runs of different chemical composition. **top left:** $Z = Z_\odot/5$, **top right:** $Z = 2.5 \times Z_\odot$, **bottom left:** C depleted ($\times 0.03$) model and **bottom right:** Fe and Si depleted ($\times 0.03$) model.

forming disk can vary, depending on $\zeta_{\rm CR}$, from $8$ to $13$ kpc , thus we could easily build a model consistent with the original stellar disk (which was cut off at $9$ kpc).

## 2.7 Discussion

The main innovation of the simulations presented in this chapter is the application of a complex ISM model to a galaxy sized object. An obvious question is to what extent the new ingredients of grain charging and ionization are really needed for a realistic model. This can be seen in the role of feedback. For model A we found that SN feedback is not needed to regulate star formation. However, we find that

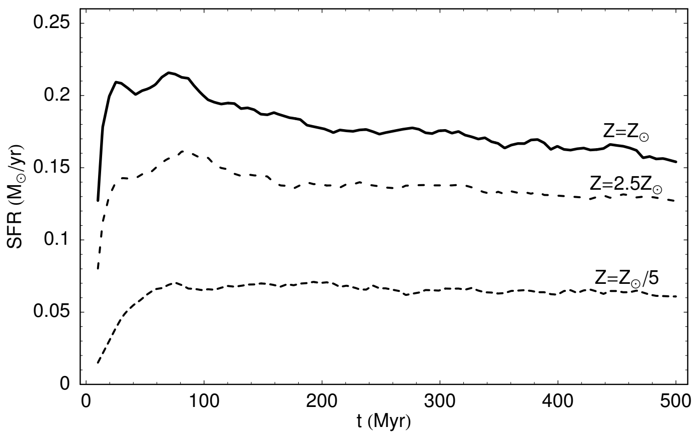


**Figure 2.17:** Star formation rate of low and high metallicity runs.

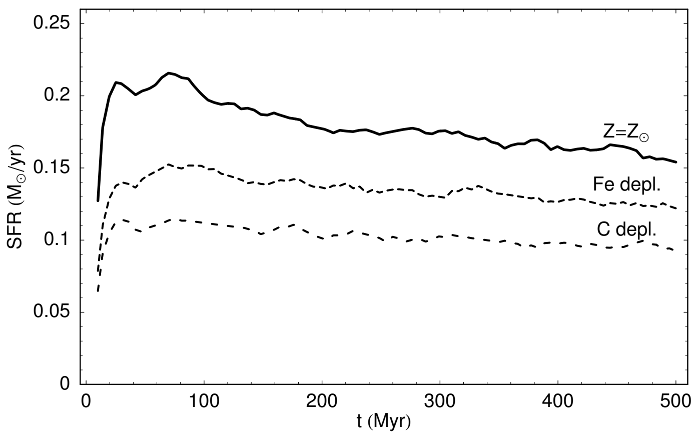


**Figure 2.18:** Star formation rate of depleted models

for realistic heating rates UV heating will not provide enough heating: in this case the temperature of heated regions will not rise above a few hundred Kelvin and SN heating becomes necessary.

It should be noted that our models are inherently limited by the numerical approach we have chosen. Obvious shortcomings of our model for the ISM are the absence of molecular gas, already discussed in section 2.3.4 and the poor representation of hot phases.

Hot tenuous phases of the ISM are a problem for SPH type codes because the mass in the hot phases is very low, so SPH, with its constant mass resolution, will by default represent low density regions poorly. Particle splitting methods may provide a way to alleviate this problem (Kitsionas & Whitworth 2002), however in our case we would also need to reassemble particles, as the gas cycles between phases.

But even the representation of the neutral phases of the ISM is hampered by resolution constraints. The cold phase can have structure roughly down to scales of the

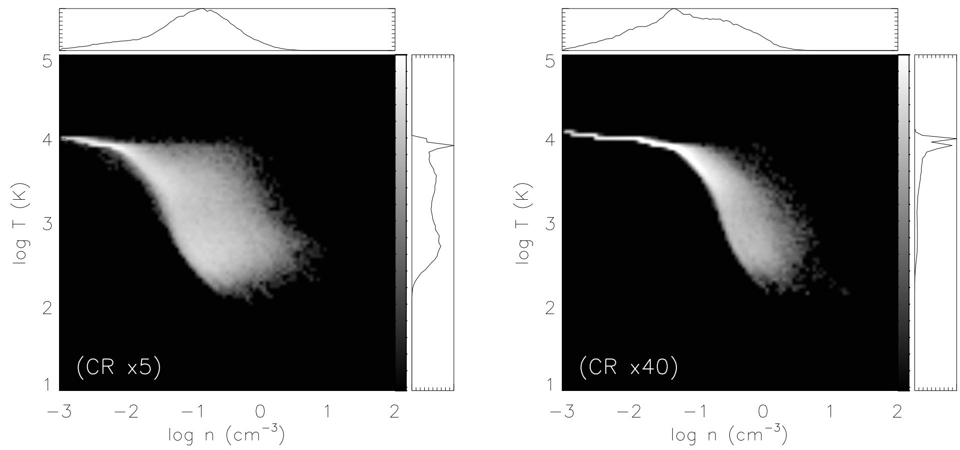


**Figure 2.19:** Temperature-density distribution of runs with higher cosmic ray fluxes (left: $\times 5$ and right: $\times 40$).

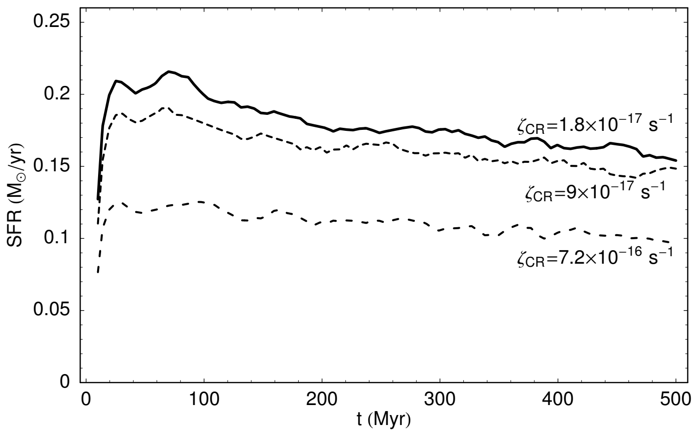


**Figure 2.20:** Star formation rate of runs with higher cosmic ray fluxes ($\times 5$ and $\times 40$).

thermal diffusion length (Meerson 1996), which can be as small as $0.1$ pc, which is below the scales we probe in our simulation. So a lot of substructure not resolved in our simulation would be present in the ISM. This can introduce errors in the cooling. Substructure will enhance the cooling by a factor ranging from anywhere from a few percent to very large values, depending on the nature of the substructure (a few percent would be for a typical random field, while for example a density field composed of polytropes of index $> 1$ would yield an unbounded factor). A more rigorous test of the effect of sub-resolution structure on the dynamics of multiphase gas would be very valuable.

Another shortcoming of the modelling is that we make the assumption of ionization equilibrium. A proper treatment of ionization could for example increase the ionization if the timescale of energy losses is shorter than the timescale for recombi-

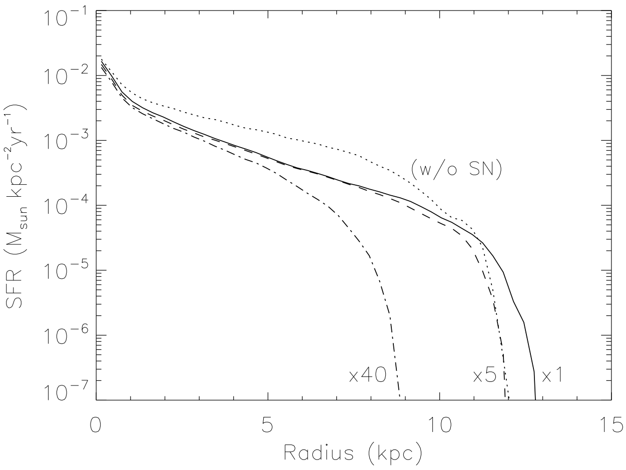


**Figure 2.21:** Star formation density as function of radius for standard runs and runs with higher cosmic ray fluxes ($\times 5$ and $\times 40$).

nation. This would result in stronger cooling in regions that are experiencing cooling from an ionized phase.

### 2.7.1 Comparison with previous work

The methods we use are comparable to those of Gerritsen & Icke (1997) and Bottema (2003). As we have noted our model A is the same as the model explored by those authors, except for the cooling curve. The fact that the cooling is different has a minor effect on the temperature structure of the gas, but the picture remains qualitatively the same. Here we have followed up on the work of Gerritsen & Icke (1997) by extending the ISM model with two important ingredients, grain charging and ionization. We find that if these two effects are taken into account, UV heating can no longer be sufficient as the sole heating source of the ISM. However their conclusions regarding structure and distribution of the gas and the truncation of star formation seem not to be affected. Our models provide a good basis to explore these phenomena further.

Bottema (2003) has explored a model for NGC 628 in some detail. He found that unless supernova feedback was added, gas would aggregate in a few large clumps distributed over the disk. We have not found a similar effect for model A, which may be due to the fact that in his simulations the resolution requirement (24) was not fulfilled.

A number of other approaches have been followed to try to simulate a star forming ISM. Springel & Hernquist (2003) formulated a sub-grid model for the multiphase interstellar medium, producing a quiescent self-regulating ISM. Some authors have tried to represent the molecular phase by formulating a phenomenological ISM model in terms of 'sticky' particles (Andersen & Burkert 2000), sometimes in addition to a SPH component representing the WNM (Semelin & Combes 2002, Berczik et al. 2003). They successfully reproduce a self-regulated ISM, including some effects, like evaporation of molecular clouds, that are probably not well represented in our model. However, these models form stars from the cloud particles imposing a Schmidt law, not, as in our model, from the consideration of the instabilities in the ISM. Furthermore, our model has a consistent representation of the ISM linking phases by physical processes, rather than prescriptions.

## 2.8 Conclusions

We have presented global models for the ISM of galaxies that include a detailed model for the neutral ISM, star formation and radiative and SN feedback. We explored the effects of different heating and cooling assumptions, chemical composition and cosmic ray fluxes using a simple template of a star forming galaxy. We have found that:

- The effect of grain charging on the photo electric heating efficiency impairs heating of the ISM. In practice this means that the heating of (diffuse) gas around young stellar clusters by UV radiation alone can not heat the ISM beyond $\approx 500$ K. As a result supernova feedback becomes more dominant.
- Solving for ionization is essential to have realistic cooling rates. A decrease in ionization rate at high densities/ low temperatures affects the cooling by atomic species.
- The effect of realistic heating and ionization act together to constrain the range of pressures of thermal instability. A decrease in metallicity, or depletion of Fe and Si extends the range.
- Star formation peaks at solar metallicities.
- Star formation is sensitive to the abundance of C, while the Fe abundance affects the relative amounts of warm and cold neutral gas.
- Our models produce a truncation radius for star formation. Cosmic ray (and X-ray) heating determines the location of this cutoff radius.

The models we have presented are of general validity, and suitable for a range of problems in galactic formation and evolution. They would be, for example, well suited to explore star formation and feedback effects for dwarf galaxies, galaxy interactions and collisions. Indeed we will study a few such applications.

# References


Andersen, R.-P. & Burkert, A., 2000, *ApJ* **531**, 296

Bakes, E. L. O. & Tielens, A. G. G. M., 1994, *ApJ* **427**, 822

Barnes, J. & Hut, P., 1986, *Nature* **324**, 446

Barnes, J. E. & Hut, P., 1989, *ApJS* **70**, 389

Bate, M. R. & Burkert, A., 1997, *MNRAS* **288**, 1060

Berczik, P., Hensler, G., Theis, C., & Spurzem, R., 2003, *Ap&SS* **284**, 865

Bottema, R., 2003, *MNRAS* **344**, 358

Bruzual A., G. & Charlot, S., 1993, *ApJ* **405**, 538

Buonomo, F., Carraro, G., Chiosi, C., & Lia, C., 2000, *MNRAS* **312**, 371

Cox, D. P., 1990, in *ASSL Vol. 161: The Interstellar Medium in Galaxies*, pp 181–200

Dalgarno, A. & McCray, R. A., 1972, *ARA&A* **10**, 375

Elmegreen, B. G., 2002, *ApJ* **577**, 206

Elmegreen, B. G. & Parravano, A., 1994, *ApJ* **435**, L121+

Field, G. B., 1965, *ApJ* **142**, 531

Gerritsen, J. P. E., 1997, *Ph.D. thesis*, Groningen University

Gerritsen, J. P. E. & Icke, V., 1997, *A&A* **325**, 972

Gingold, R. A. & Monaghan, J. J., 1977, *MNRAS* **181**, 375

Habing, H. J., 1968, *Bull. Astron. Inst. Netherlands* **19**, 421

Heiles, C. & Troland, T. H., 2003, *ApJ* **586**, 1067

Hernquist, L., 1993, *ApJS* **86**, 389

Hernquist, L. & Katz, N., 1989, *ApJS* **70**, 419

Kanekar, N., Subrahmanyan, R., Chengalur, J. N., & Safouris, V., 2003, *MNRAS* **346**, L57

Katz, N., 1992, *ApJ* **391**, 502

Kitsionas, S. & Whitworth, A. P., 2002, *MNRAS* **330**, 129

Kuijken, K. & Dubinski, J., 1995, *MNRAS* **277**, 1341

Lamers, H. J. G. L. M., Panagia, N., Scuderi, S., Romaniello, M., Spaans, M., de Wit, W. J., & Kirshner, R., 2002, *ApJ* **566**, 818

Le Bourlot, J., Pineau des Forêts, G., & Flower, D. R., 1999, *MNRAS* **305**, 802

Leitherer, C., Schaerer, D., Goldader, J. D., Delgado, R. M. G., Robert, C., Kune, D. F., de Mello, D. F., Devost, D., & Heckman, T. M., 1999, *ApJS* **123**, 3

Lucy, L. B., 1977, *AJ* **82**, 1013

Mac Low, M. & Klessen, R. S., 2004, *Rev. of Mod. Phys.* **76**, 125

Makino, J., Fukushige, T., Koga, M., & Namura, K., 2003, *PASJ* **55**, 1163

McCall, B. J. et al., 2003, *Nature* **422**, 500

Meerson, B., 1996, *Rev. of Mod. Phys.* **68**, 215

Mellema, G. & Lundqvist, P., 2002, *A&A* **394**, 901

Monaghan, J. J., 1992, *ARA&A* **30**, 543

Monaghan, J. J. & Lattanzio, J. C., 1985, *A&A* **149**, 135

Navarro, J. F., Frenk, C. S., & White, S. D. M., 1997, *ApJ* **490**, 493

Navarro, J. F. & White, S. D. M., 1993, *MNRAS* **265**, 271

Nelson, R. P. & Papaloizou, J. C. B., 1993, *MNRAS* **265**, 905

Nelson, R. P. & Papaloizou, J. C. B., 1994, *MNRAS* **270**, 1

Parravano, A., Hollenbach, D. J., & McKee, C. F., 2003, *ApJ* **584**, 797

Raga, A. C., Mellema, G., & Lundqvist, P., 1997, *ApJS* **109**, 517

Rasio, F. A., 1999, *arXiv:astro-ph/9911360* p. 13

Richter, P., Sembach, K. R., Wakker, B. P., & Savage, B. D., 2001, *ApJ* **562**, L181

Salmon, J. K. & Warren, M. S., 1994, *Journal of Computational Physics* **111**, 136

Schaye, J., 2004, *ApJ* **609**, 667

Schmidt, M., 1959, *ApJ* **129**, 243

Semelin, B. & Combes, F., 2002, *A&A* **388**, 826

Shu, F. H., Adams, F. C., & Lizano, S., 1987, *ARA&A* **25**, 23

Silich, S. A., Franco, J., Palous, J., & Tenorio-Tagle, G., 1996, *ApJ* **468**, 722

Silva, A. I. & Viegas, S. M., 2001, *Computer Physics Communications* **136**, 319

Springel, V. & Hernquist, L., 2002, *MNRAS* **333**, 649

Springel, V. & Hernquist, L., 2003, *MNRAS* **339**, 289

Springel, V., Yoshida, N., & White, S. D. M., 2001, *New Astronomy* **6**, 79

Sutherland, R. S. & Dopita, M. A., 1993, *ApJS* **88**, 253

van Dishoeck, E. F. & Black, J. H., 1986, *ApJS* **62**, 109

Voronov, G. S., 1997, *Atomic Data and Nuclear Data Tables* **65**, 1

Watson, W. D., 1972, *ApJ* **176**, 103

Webber, W. R., 1998, *ApJ* **506**, 329

Whitworth, A. P., 1998, *MNRAS* **296**, 442

Wolfire, M. G., Hollenbach, D., McKee, C. F., Tielens, A. G. G. M., & Bakes, E. L. O., 1995, *ApJ* **443**, 152

Wolfire, M. G., McKee, C. F., Hollenbach, D., & Tielens, A. G. G. M., 2003, *ApJ* **587**, 278

Zuckerman, B. & Evans, N. J., 1974, *ApJ* **192**, L149